IEEE Access
Multidisciplinary : Rapid Review : Open Access Journal

Received 18 December 2024, accepted 5 January 2025, date of publication 7 January 2025, date of current version 13 January 2025.

Digital Object Identifier 10.1109/ACCESS.2025.3526890

RESEARCH ARTICLE

Optimally Located Subconductors and Phases to Achieve Transmission Lines With High Natural Power and Narrow Corridor Width

MUSHFIQUL ABEDIN KHAN, (Graduate Student Member, IEEE),
EASIR ARAFAT, (Graduate Student Member, IEEE), **SAIKAT CHOWDHURY**, (Member, IEEE),
AND MONA GHASSEMI, (Senior Member, IEEE)
Zero Emission, Realization of Optimized Energy Systems (ZEROES) Laboratory, The University of Texas at Dallas, Richardson, TX 75080, USA
Department of Electrical and Computer Engineering, The University of Texas at Dallas, Richardson, TX 75080, USA

Corresponding author: Mona Ghassemi (mona.ghassemi@utdallas.edu)

This work was supported in part by the National Science Foundation under Award 2306098.

ABSTRACT The number and location of subconductors in an overhead transmission line affect its inductance and capacitance, leading to a change in its natural power. Traditionally, for conventional transmission lines around above 300 kV, more than one conductor has been used as bundles for each phase. The subconductors in these bundles have been placed in a symmetrical arrangement in space. Conventional high-natural power lines are designed to have a greater number of subconductors per bundle and a greater bundle radius than a conventional line at the same voltage level. In this paper, new configurations with various numbers of subconductors for unconventional high natural power line designs are studied. The term ''unconventional'' denotes that the subconductors are not arranged in space in the traditional symmetrical configurations used in the conventional lines and conventional high natural power lines mentioned above. Instead, their optimized locations are found so that their natural power can be further increased. The aim is to enhance the natural power of these new line designs via optimally located subconductor configurations to achieve narrower corridor width as well. Moreover, for these optimally designed transmission lines, 1) corona loss, 2) audible noise, 3) radio and television interferences, 4) location of shield wires, and 5) electric and magnetic fields under these lines are calculated and compared with them for conventional lines. It has been shown that for our newly designed unconventional line with $N = 8$, the SIL achieved is 1414.70 MW, which is a 43% increase compared to that of the conventional line; and the reduced line width of 9.7 m is only 40% of that of the conventional line. Consequently, this leads to the mentioned unconventional line having a natural power density of 3.38 times that of the conventional line.

INDEX TERMS Natural power, transmission lines, subconductors, line design.

I. INTRODUCTION

The electric power sector has grown into a horizontally integrated business, primarily focusing on bringing forth innovation, particularly in the generation and distribution industries, in the past decades. In the generation sector, a transformation from large synchronous machines to much smaller and lighter generators and the inclusion of renewable energy has been witnessed. The distribution sector has seen a rise in electronic converters and power-saving ways in industries and homes. In the case of the transmission sector, which provides the highways of energy transfer in the system, the scope for improvement is still there.

The primary constraints in the transmission sector originate from transmission lines either directly, such as thermal limit, or indirectly, such as voltage drops in buses and different types of stabilities. For transmission voltage levels (> 300 kV) and usual transmission networks with lots of branches, however, loaded heavily, voltage drop limit at buses often plays as the dominant limit. Various reactive

The associate editor coordinating the review of this manuscript and approving it for publication was Diego Bellan.

power compensation apparatuses have been developed and implemented, from fixed shunt capacitors/reactors and series capacitors to FACTS. However, the main drawbacks to all these techniques are that they are costly and add technical challenges to the system, especially regarding their control and protection [1].

Regarding trends toward net zero emission has led to more use of renewable energies. For example, it is expected that by 2030 approximately 300 GW, and by 2050 about 1.5 TW of wind and solar power will be introduced into the US grid [2]. For this to be effectively integrated into existing power grids, high voltage transmission capacity must be increased by 60% by 2030 and triple by 2050 – the required investment for this is 360 billion USD up until 2030 and 2.4 trillion USD by 2050 [2]. The main issue is that extra high voltage (EHV) transmission lines are costly. Based on [3], the cost for a new single circuit transmission line at 500 kV in different US states ranges from \$4.1M/mile in Montana, North Dakota, and South Dakota to \$5.1M/mile in Louisiana. In such a situation, developing optimal designs for transmission lines leading to the need for fewer transmission lines for transmission expansion planning (TEP) can lead to remarkable savings as shown in [4] and [5], and this is precisely the goal of this paper. In general, these lines are designed to have smaller inductance and larger capacitance than conventional lines, and as a result, they can naturally provide reactive compensation. These optimally designed lines often lead to narrower towers, which is another merit regarding the existing and increasing challenges for line's right-of-ways.

In this paper, an algorithm is developed to figure out the optimized positions of subconductors toward maximizing lines's natural power as much as possible. In this regard, key constraints such as the minimum phase distance, maximum electric field on subconductors, and limits on the height of subconductors are considered. Then, for the optimized designs, other electrical aspects of the line design, such as corona loss, audible noise, radio and television noises, and electric and magnetic fields under these lines, are calculated, and the results are compared with those from a conventional line. Note that involving all electrical aspects of the line design to determine the optimal location of subconductors leads to a complex problem. Based on our experience, optimally designed line configurations considering the key constraints mentioned above often meet other electrical aspects mentioned above.

II. METHOD

A. OPTIMAL LOCATION OF SUBCONDUCTORS

Conventional lines have a traditional circular bundle arrangement. However, in our study, we focused on unconventional arrangements that break the circular symmetry to achieve higher natural power, P_n, values. Since we are using a more number of subconductors to reach higher P_n values, to keep the cost low, the cross-section of the conductor is chosen such that it is lower than that of the one used in conventional lines. The design has been made based on the following constraints.

It must be ensured for each of the phases, $i \in \{1, 2, 3\}$, that the maximum corresponding electric field, E_i^{max}, on the conductor surface is within a particular limiting value, E_{th}, i.e., a threshold that is introduced in the first constraint, Eq. (1). The value of E_{th} considered here is 20 kV/cm.

$$E_i^{max} < E_{th}, i \in \{1, 2, 3\} \tag{1}$$

The phase-to-phase and the phase-to-ground distances must also be greater than the minimum clearance required for each, Eqs. (2) and (3).

$$D_{ij}^{ph-ph} > D_{min,ph-ph}, i, j \in \{1, 2, 3\} \,\&i \neq j \tag{2}$$

$$H_i^{ph-gnd} > H_{min,ph-gnd}, i \in \{1, 2, 3\} \tag{3}$$

To start the search for optimal subconductor locations, the electric field strength on subconductor surface is first found for a base scenario where the positions are selected based on an initial set of values for the phase-to-phase and phase-to-ground distances. E_i^{max} is then found from these field values for the corresponding subconductors in each phase. The locations are adjusted as long as the first constraint, Eq. (1), is met. Subsequently, line capacitance and inductance, and P_n are determined. Capacitance equalization, as explained in [1], is performed to make the search process faster by finding points close to the optimum locations of the subconductors. E_i^{max} value is found again, this time by setting boundary conditions where the minimum distance between phases, $D_{min,ph-ph}$ is set and the maximum and the minimum allowable heights for the conductors are also set. The value of $D_{min,ph-ph}$ is increased gradually until the first constraint is satisfied again, and then the line parameters are calculated. If the updated P_n is lower than before, a new set of points is considered, and the process is repeated.

B. ELECTRIC FIELD CALCULATION

The conventional method for determining the conductor surface electric field involves calculating Maxwell's potential coefficients and subsequently obtaining the necessary values. Each conductor is modeled with a single line charge, which allows the use of $q = CV$, where q, C, and V are the stored charge in the subconductors, the capacitance, and the potential difference respectively. It can then be rewritten to give $[P]\,[q] = [V]$ for n subconductors. Here $[P]$ is Maxwell's Potential matrix of size $(n.m) \times (n.m)$, where m is the number of phases. The elements of $[P]$ are found as follows:

$$P_{ii} = \frac{1}{2\pi\epsilon_0} \ln \frac{2H_i}{r_i} \tag{4}$$

$$P_{ij} = \frac{1}{2\pi\epsilon_0} \ln \sqrt{1 + 4\frac{H_i H_j}{D_{ij}^2}} \tag{5}$$

where H_i represents the average height, r_i is the radius of subconductor i, and D_{ij} is the distance between subconductors i and j. However, this method does not account for the asymmetrical configuration of unconventional high natural power lines targeted in this paper or the effect of other subconductors around. Thus, a new approach was considered for our purposes [6]. Here, each of the subconductors with radius $\vec{r_p}$ is represented using N_p line charges, distributed around an imaginary cylinder with radius $\vec{r_i} = r/2$, and centered on the conductor's axis to establish the electric potential at N_p points on the subconductor surface. The surface potential for each point p can be found using:

$$E(p) = \frac{1}{2\pi\varepsilon_0}\sum_{i=1}^{N\mathrm{x}N_p}\frac{q_i}{\left|\vec{r_p}-\vec{r_i}\right|^2}\left(\vec{r_p}-\vec{r_i}\right) \tag{6}$$

where, q_i is the charge on subconductor i. Fig. 1 shows the modeling of subconductors with this new approach.

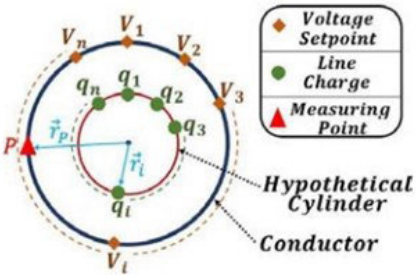

FIGURE 1. Modeling of conductors with N_p line charges.

The results from this method have been validated by COMSOL Multiphysics.

III. CASE STUDIES

In our investigation, we have taken into account existing 3-phase, 500 kV conventional lines and conventional high natural power lines. We have also attempted to develop and study an innovative, unconventional, high-natural power line designed for the same voltage level. To the best of our knowledge, G. N. Alexandrov was the first to introduce non-circular conductor bundle arrangements to increase the capacity of transmission lines [7] and later was also studied by others [8], [9], [10], [11]

A. CONVENTIONAL LINE AND CONVENTIONAL HIGH NATURAL POWER LINES

The 500 kV, 3-phase conventional line considered and shown in Fig. 2a consists of bundled subconductors arranged in a horizontal configuration. The conductor bundles consist of 4 subconductors, each having a diameter of 26.82 mm and a bundle spacing of 0.45 m, symetrically located on a circle. For this line, the phase spacing is 12.3 m, and the height of the phase conductors is 28 m from the ground.

The conventional high natural power line considered here has 6-subconductor bundles shown in Fig. 2b, which are placed in an inverted delta configuration. The subconductors in the bundle are distributed with equal bundle spacings, resulting in a symmetrical shape. The diameter of the subconductors is 21.60 mm, and the bundle radius is 0.375 m. The phase spacing for this line is Dph=6.7 m, and the central phase is 27.5 m from the ground surface.

Both the lines shown in Fig. 2 are actual lines and are in service [11], where Table 1 presents their natural power or surge impedance loading (SIL) and corridor width, i.e., the distance between the outer phase conductors.

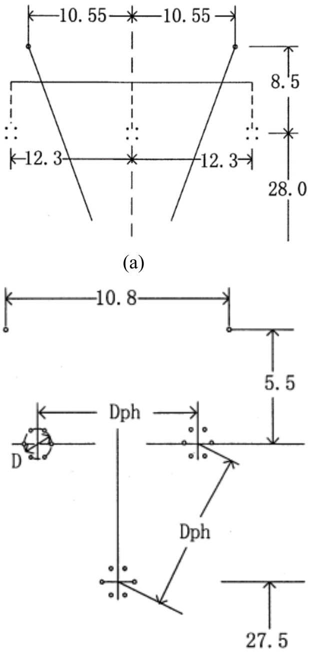

(a)

(b)

FIGURE 2. Line configuration of the 500 kV (a) conventional line and (b) conventional high natural power line.

TABLE 1. Line data for the conventional line and the conventional high natural power lines.

	Phase Configuration	N	SIL (MW)	Corridor Width (m)
Conventional Line (Fig. 2a)	Horizontal	4	989.29	24.60
Conventional High Natural Power Line (Fig. 2b)	Inverted Delta Configuration	6	1332	6.70

B. UNCONVENTIONAL HIGH NATURAL POWER LINES

Using our formulated method, we have derived locally optimized subconductor configurations aimed at achieving increased SIL. This yields unconventional high natural power lines characterized by subconductor arrangements that deviate from the symmetrical configurations typically seen in conventional lines. Our developed lines have bundles consisting of 4 to 8 subconductors. With each incremental increase in the number of subconductors, a conductor having a smaller cross-section is considered to mitigate the increase in cost due to the increased number of subconductors. The details of these conductors are given in Table 2.

IV. RESULTS

A. OPTIMALLY DESIGNED UNCONVENTIONAL HIGH NATURAL POWER LINES

In this section, we have presented the novel configurations of unconventional high natural power lines, explored the impact

TABLE 2. Conductor type of unconventional high natural power lines.

N	Subconductor Name	Diameter (in)
4	Catbird	1.140
5	Stilt	1.036
6	Eagle	0.953
7	Hawk	0.858
8	Tailorbird	0.825

of corona discharge, and drawn a comparison with the lines shown in Fig. 2. Under the mentioned constraints, the restructured lines have shown considerable improvement over the conventional line, Fig. 2a, in terms of having higher SIL, narrower lines and higher power density. We also designed conventional high-natural power lines and considered them for comparison. For each of these conventional high natural power line configurations, the bundle radius is held constant at 0.3182 m, which is the same as that in the conventional line shown in Fig. 2a; and the minimum distance from the subconductors of one phase to those of the other phases is kept greater than or equal to 6.7 m. This amount is based on the line shown in Fig. 2b, and as a result, the line width for each of the conventional high natural power lines is 7.34 m. The minimum distance of 6.7 m between phases is also maintained for our optimally designed unconventional high natural power lines.

The optimally designed lines mentioned above are presented in Table 3. Figs. 3a-3e show the optimally designed unconventional 500-kV lines configurations for a number of subconductors, N, equal to 4, 5, 6, 7, and 8, respectively. Fig. 3f geometrically compares the conventional line, Fig. 2a, with the optimally designed unconventional one with N=8.

TABLE 3. Conventional and unconventional high natural power lines.

	Unconventional high natural power lines			Conventional high natural power lines	
N	SIL (MW)	Line width (m)	E_{max} (kV/cm)	SIL (MW)	E_{max} (kV/cm)
4	1277.70	10.00	20.02	1160.65	15.93
5	1377.30	12.34	18.56	1199.69	14.85
6	1413.10	12.07	18.70	1225.49	14.02
7	1404.70	11.67	19.29	1241.98	13.69
8	1414.70	9.70	19.73	1256.72	12.87

As mentioned before, electric field intensity on subcnductors is calculated via the method described in Section II.B. The method as mentioned before again was validated with results from COMSOL Multiphysics. Here for example, the maximum electric field on the surface of the subconductor for the unconventional line with N=8 using our method, as shown in Table 3 is 19.73 kV/cm and that found using COMSOL Multiphysics is 19.733 kV/cm as shown in Fig. 4, thus validating our novel method for electric field calculation.

As seen from Table 3, the natural power for the optimally designed unconventional line with N=8 is 1414.70 MW which is 43% more than that for the conventional line, Fig. 2a, and 12.5% more than that for the conventional high natural power line with N=8, showing the unconventional design can result to higher natural power at the same condition. Moreover, the line width for the mentioned unconventional line is only 9.7 m which is 40% of that for the conventional line and 75% of that for the mentioned conventional high natural power line. Combining the numbers from natural power and line width mentioned above results in 3.38 times higher natural power density than the conventional line and 1.5 times higher natural power density than the conventional high natural power line. All these show the potential of the optimally designed unconventional high natural power lines as a game changer in transferring bulk power in future power grids. In the following sections, other electrical aspects of the line design for the optimally designed unconventional lines described above are calculated and compared with the conventional line.

B. MAGNETIC FIELD UNDER LINES

It is an important factor to evaluate the magnetic field under transmission lines in the vicinity of the right of way. It should be under a desired value and this value may vary from country to country or even may be different in different states or provinces of a country.

While carrying 50 or 60 Hz current in a transmission line magnetic field is generated in its surroundings. For a fixed N_c number of horizontal conductors, the magnetic field considering the induced eddy current can be obtained by [12] and [13]:

$$B_{rms} = 0.2 \times \sum_{n=1}^{N_c} I_n \left\{ \left[\frac{(y-d_n)}{r_{cn}^2} - \frac{(y+d_n+\alpha)}{r_{in}^2} \right] \vec{a}_x - \left[\frac{(x-h_n)}{r_{cn}^2} - \frac{(x-h_n)}{r_{in}^2} \right] \vec{a}_y \right\} \mu T$$

$$r_{cn} = \sqrt{(x-h_n)^2 + (y-d_n)^2}$$
$$r_{in} = \sqrt{(x-h_n)^2 + (y+d_n+\alpha)^2}$$
$$\alpha = \sqrt{2}\delta_g e^{-j\pi/4}, \quad \delta_g = 503\sqrt{\rho_g/f} \tag{7}$$

where ρ_g is denoting earth resistivity $(\Omega.m)$, f is denoting the frequency in Hz, I_n is denoting the conductor current (Amps-rms), and all distances are considered in meters. The n-th conductor is positioned at $(x, y) = (h_n, d_n)$. The earth current matches in magnitude and runs in the opposite direction for each conductor. For the image current property, each earth current is buried in the earth with a complex depth proportional to δ_g, the earth's skin depth.

Figs. 5a shows a comparison between the real-life measured magnetic field values under a line and computed ones from [12]. Fig. 5b shows the reproduced results using our code for Eq. (7) which validates our code.

For computing magnetic fields under transmission lines, especially for unconventional bundle arrangements targeted

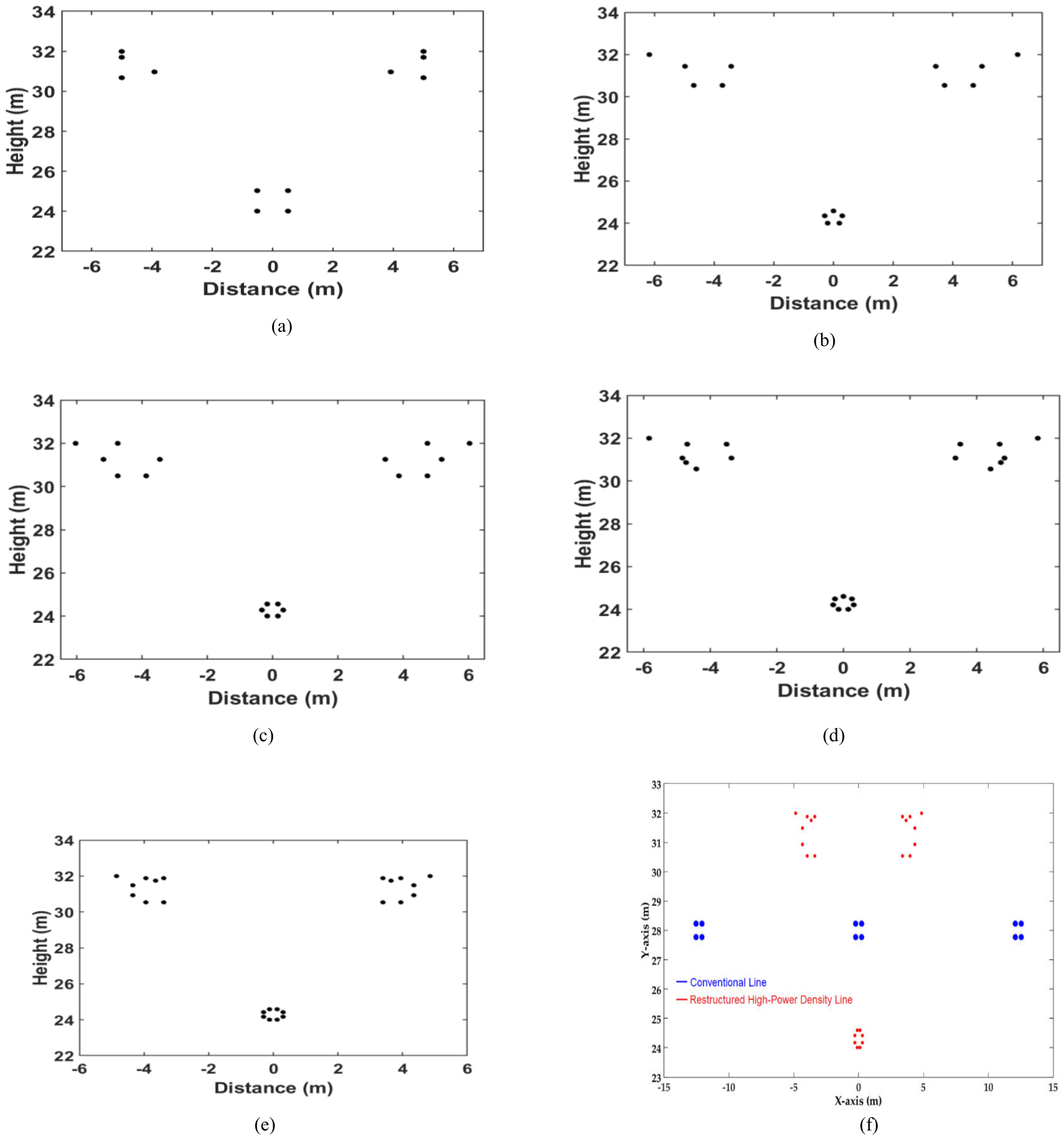

(a)

(b)

(c)

(d)

(e)

(f)

FIGURE 3. Line configurations of the 500 kV unconventional lines with (a) $N = 4$, (b) $N = 5$, (c) $N = 6$, (d) $N = 7$, (e) $N = 8$, and (f) comparison of the unconventional line with $N = 8$ against the conventional line.

in this paper, we need to consider each subconductor separately while to date an equivalent conductor carrying phase current in the middle of the bundle circle was considered for conventional lines. Considering each subconductor separately leads to more accurate results.

To make a comparison of the magnetic fields resulting from the conventional line, shown in Fig. 2a, and the unconventional line, shown in Fig. 3e, we considered that both lines carry the same phase current. The magnetic field profiles were calculated at ground level, Fig. 6a, and 1 m above the ground level, Fig. 6b. As seen in Fig. 6, the magnetic field for the unconventional line is well lower than the conventional line, another merit for these new line configurations.

C. ELECTRIC FIELD UNDER LINES

As a three-phase system, three alternating voltages (of the same frequency) are carried by three circuit wires and reach their instantaneous peak levels one-third of a cycle apart.

As a single circuit 3-phase line, consider the line voltage as $[V]$ that is related to the peak amplitude V_m, initial angle

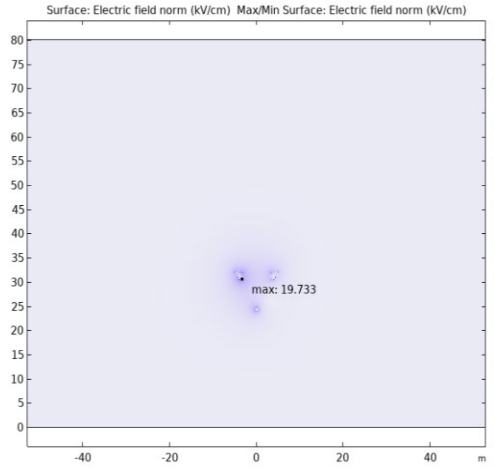

FIGURE 4. **Maximum electric field on the surface of the subconductor for the unconventional line with N=8.**

ϕ and the angular frequency ω and presented in Eq. (8).

$$[V] = V_m \left[\sin(\omega t + \phi), \sin\left(\omega t + \phi + 120^\circ\right), \sin\left(\omega t + \phi + 120^\circ\right)\right] \tag{8}$$

Let, J and K are horizontal and vertical coefficients that determine the electric field at a certain point, calculated by Eqs. (9) and (10), [14]. The other parameters of these equations are mentioned in Fig. 7.

$$J_i = (y - y_i)\left(\frac{1}{r_i^2} - \frac{1}{\left(r_i'\right)^2}\right) \tag{9}$$

$$K_i = \left(\frac{(z - z_i)}{r_i^2} - \frac{(z + z_i)}{\left(r_i'\right)^2}\right) \tag{10}$$

Then

$$\begin{aligned} E_{v1} &= \left(\frac{q_1}{2\pi\epsilon_0}\right) K_1 \\ &= V_m.K_1 \left[M_{11}\sin(\omega t + \phi) \right. \\ &\quad + M_{12} sin\left(\omega t + \phi - 120^\circ\right) \\ &\quad \left. + M_{13}\sin\left(\omega t + \phi + 120^\circ\right)\right] \end{aligned} \tag{11}$$

$$\begin{aligned} E_{v2} &= \left(\frac{q_2}{2\pi\epsilon_0}\right) K_2 \\ &= V_m.K_2 \left[M_{21}\sin(\omega t + \phi) \right. \\ &\quad + M_{22} sin\left(\omega t + \phi - 120^\circ\right) \\ &\quad \left. + M_{23}\sin\left(\omega t + \phi + 120^\circ\right)\right] \end{aligned} \tag{12}$$

$$\begin{aligned} E_{v3} &= \left(\frac{q_3}{2\pi\epsilon_0}\right) K_3 \\ &= V_m.K_3 \left[M_{31}\sin(\omega t + \phi) \right. \\ &\quad + M_{32} sin\left(\omega t + \phi - 120^\circ\right) \\ &\quad \left. + M_{33}\sin\left(\omega t + \phi + 120^\circ\right)\right] \end{aligned} \tag{13}$$

Then, the total vertical component is

$$\begin{aligned} E_{vn} = V_m &[(K_1 \cdot M_{11} + K_2 \cdot M_{21} + K_3 \cdot M_{31}) \\ &\sin(\omega t + \phi) \\ &+ (K_1 \cdot M_{12} + K_2 \cdot M_{22} + K_3 \cdot M_{32}) \\ &\sin\left(\omega t + \phi - 120^\circ\right) + (K_1 \cdot M_{13} + K_2 \cdot M_{23} + K_3 \cdot M_{33}) \\ &\sin\left(\omega t + \phi + 120^\circ\right)] \\ = V_m &\left[K_{v1}\sin(\omega t + \phi) + K_{v2}\sin\left(\omega t + \phi - 120^\circ\right) + K_{v3} \right. \\ &\left. \sin\left(\omega t + \phi + 120^\circ\right)\right] \end{aligned}$$

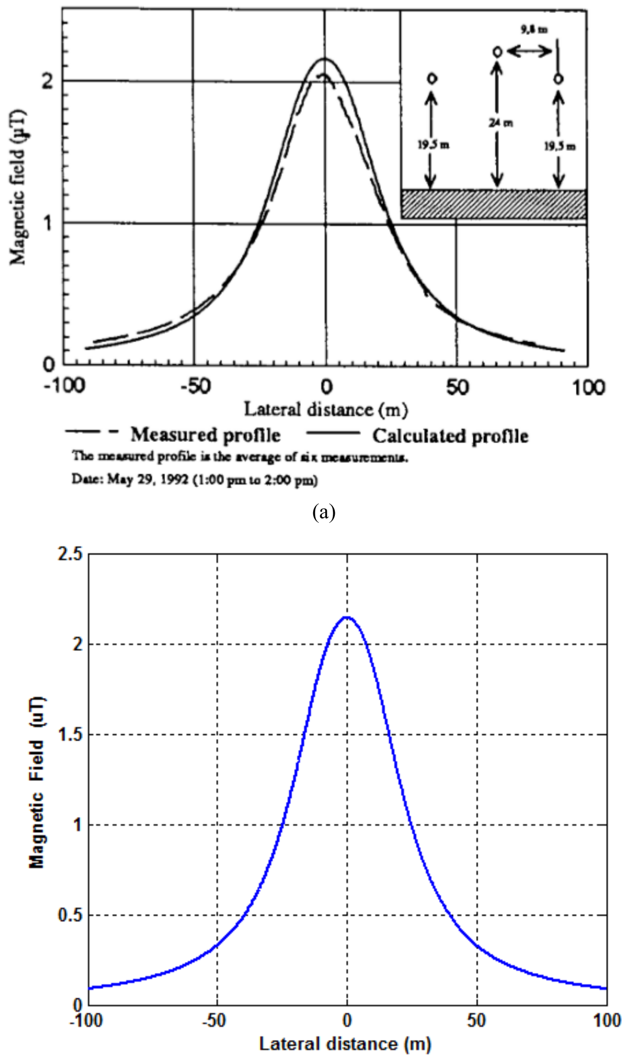

The measured profile is the average of six measurements.
Date: May 29, 1992 (1:00 pm to 2:00 pm)

(a)

(b)

FIGURE 5. **(a) Magnetic fields for a 735 kV overhead line, (280 A) from [12], (b) magnetic fields calculated by the code written for this paper.**

and in phasor form,

$$\begin{aligned} E_{vn} = V_m &\left[K_{v1}\angle\phi + K_{v2}\angle\left(\phi - 120^\circ\right)\right. \\ &\left. + K_{v3}\angle\left(\phi + 120^\circ\right)\right] \end{aligned} \tag{14}$$

Resolving Eq. (14) into real and imaginary parts with $\phi = 0$, we obtain

$$\left.\begin{aligned} real\ part &= K_{v1} - 0.5\,K_{v2} - 0.5\,K_{v3} \\ imaginary\ part &= 0 - 0.866\,K_{v2} + 0.866\,K_{v3} \end{aligned}\right\} \tag{15}$$

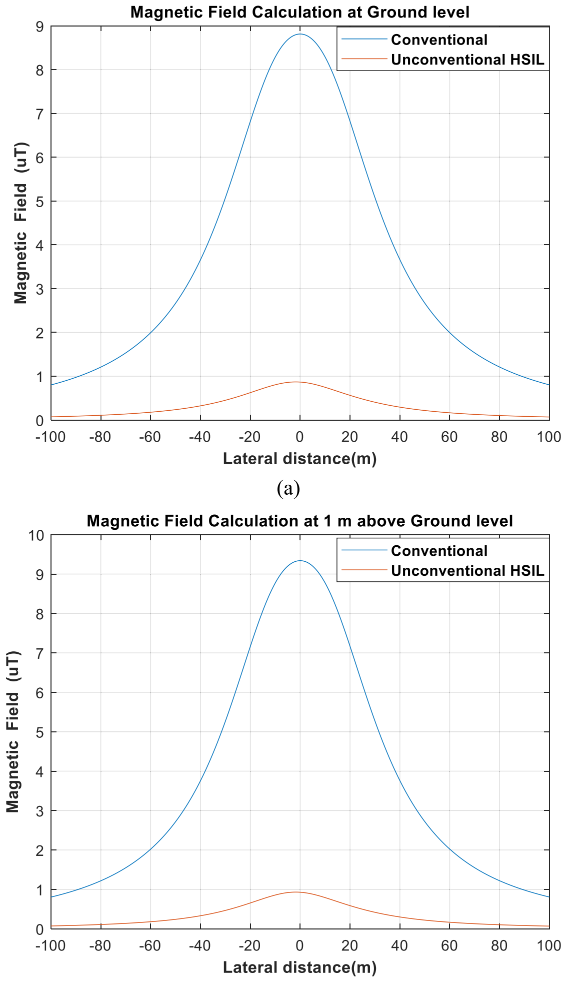

(a)

(b)

FIGURE 6. Magnetic field profiles under the transmission lines (a) at ground level, (b) at 1 m above the ground level.

Consequently, the amplitude of the electric field is:

$$\hat{E}_{vn} = \sqrt{\left[(K_{v1} - 0.5\,K_{v2} - 0.5\,K_{v3})^2 + 0.75\,(K_{v3} - K_{v2})^2\right]} \cdot V_m = \sqrt{{K_{v1}}^2 + {K_{v2}}^2 + K_{v3}^2 - K_{v1}K_{v2} - K_{v2}K_{v3} - K_{v3}K_{v1}} \cdot V_m = K_v \cdot V_m$$

The r.m.s. value of the total vertical component at $P\,(x, y)$ due to all 3 phases will be

$$E_{vn} = \frac{\hat{E}_{vn}}{\sqrt{2}} = K_v \cdot V \tag{16}$$

In a similar manner, the r.m.s. value of a total horizontal component of the field at P due to all 3 phases is

$$E_{hn} = J_h \cdot V = V \cdot \sqrt{J_{h1}^2 + J_{h2}^2 + J_{h3}^2 - J_{h1}J_{h2} - J_{h2}J_{h3} - J_{h3}J_{h1}} \tag{17}$$

where

$$\left.\begin{aligned} J_{h1} &= J_1 \cdot M_{11} + J_2 \cdot M_{21} + J_3 \cdot M_{31} \\ J_{h2} &= J_1 \cdot M_{12} + J_2 \cdot M_{22} + J_3 \cdot M_{32} \\ J_{h3} &= J_1 \cdot M_{13} + J_2 \cdot M_{23} + J_3 \cdot M_{33} \end{aligned}\right\} \tag{18}$$

where the values of J_1, J_2, J_3 are obtained from Eq. (9) for J_i with $i = 1, 2, 3$.

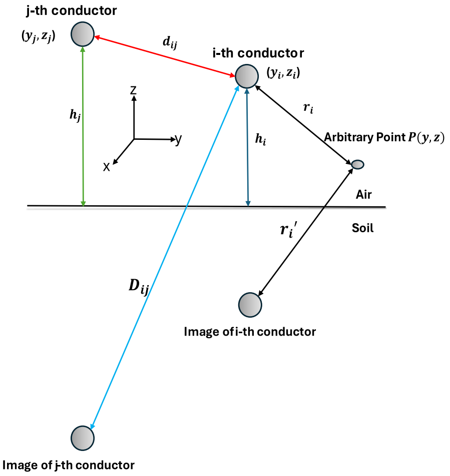

FIGURE 7. The distances between the point charges, their images, and a chosen point.

Like the magnetic field calculation, we have considered each subconductor separately to evaluate the electric field under the transmission lines. Figs. 8a and 8b show the electric field under the conventional line shown in Fig. 2a and the unconventional line shown in Fig. 3e for a height of 1 m above the ground level and at the ground level, respectively. As seen in Fig. 8, the unconventional line result is well lower electric field at the vicinity of the right of way of the line than the conventional line, another merit for these unconventional high natural power lines.

D. CORONA LOSS

The empirical formula for corona power loss under foul weather in kW/mile by Bonneville Power Administration (BPA) considers E_{max} on subconductors, the subconductor diameter d, number of subconductors N, and the altitude A, and is given by [15], [16], [17], and [18].

$$P = 1.60934 \times 3 \times 10^{\frac{14.2 + 65\log\left(\frac{E_{max}}{18.8}\right) + 40\log\left(\frac{d}{3.51}\right) + K_1\log\left(\frac{N}{4}\right) + K_2 + \frac{A}{300}}{10}} \tag{19}$$

where K_1 and K_2 are parameters depending on the rainfall rate.

An alternative empirical formula from project EHV shows that [19].

$$P = P_{FW} + \left[\frac{V}{\sqrt{3}} J r^2 \ln\left(1 + KR\right)\right] \sum_{1}^{3N} E^5 \tag{20}$$

where P_{FW}, J, K, R represent the fair-weather corona loss, a loss current constant, wetting coefficient, and the rainfall

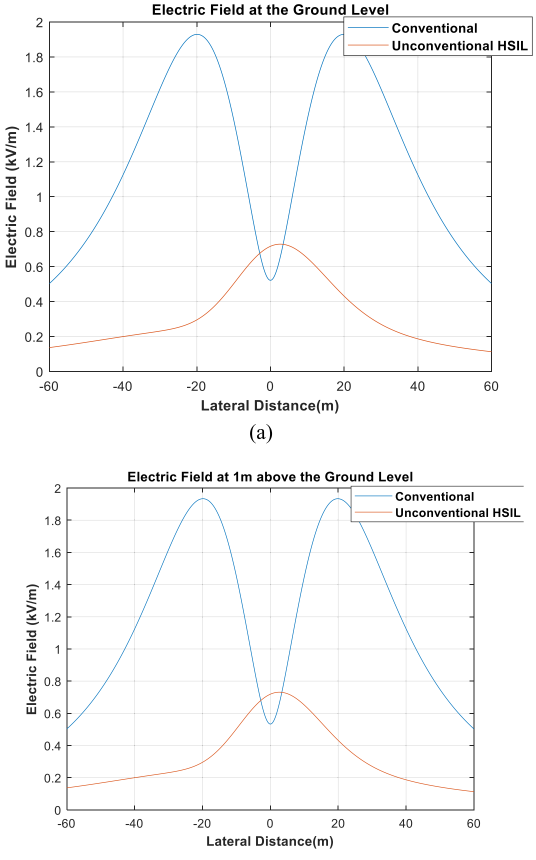

(a)

(b)

FIGURE 8. **Electric field profiles under the transmission lines (a) at ground level, (b) at 1 m above the ground level.**

rate, respectively. E is the conductor underside surface voltage gradient in kV/cm. The fair-weather corona loss can be calculated from Eq. (2) by subtracting 17 dB from the mean foul-weather corona loss, or by the Électricité de France (EDF) formula as follows [15].

$$P = P_0 r^{1.8} \left(N+6\right)^2 .10^{7\left(E^*-0.7\right)} W/m \tag{21}$$

The power loss due to corona discharge in fair and rainy weather has been evaluated using Eqs. (19), (20), and (21). The fair-weather corona loss for the transmission lines under study has been shown in Table 4.

TABLE 4. **Fair-weather corona power loss for various overhead transmission lines.**

	BPA (kW/mile)		EDF (W/m)
	Altitude = 0 m	Altitude = 1000 m	
Conventional	0.398	0.728	0.276
Conventional HSIL	1.484	3.197	2.781
Unconventional HSIL, N=8	1.853	3.993	2.481

Fig. 9 shows the corona loss in rainy weather for the conventional, conventional high natural power or high SIL (HSIL), and unconventional HSIL lines found using the empirical formula developed in Project EHV. The significant difference in the calculated corona loss in rainy weather conditions for rain rates greater than 0.1 in/h is seen in Fig. 10, where the results have been evaluated using both Eq. (19) and Eq. (20). Fig. 11 shows the corona loss for all three lines for an altitude of 1000 m. A significant rise in power loss is seen due to the increase in altitude. The unconventional HSIL line shows the highest loss values, followed by the conventional HSIL line and the conventional line. Figs. 9-11 also show a rapid initial rise in the corona loss with rainfall rates of small values; as the rain rate increases, the loss level gradually reaches saturation. Similar results have been obtained for the conventional line and the unconventional HSIL line in [20].

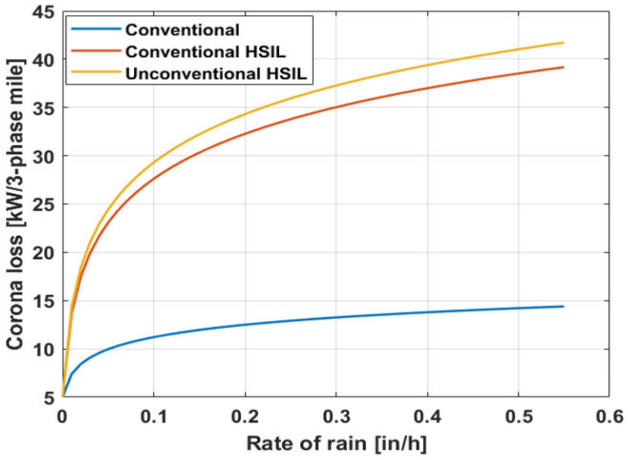

FIGURE 9. **Corona power loss in overhead transmission lines against rain rate using Eq. (20).**

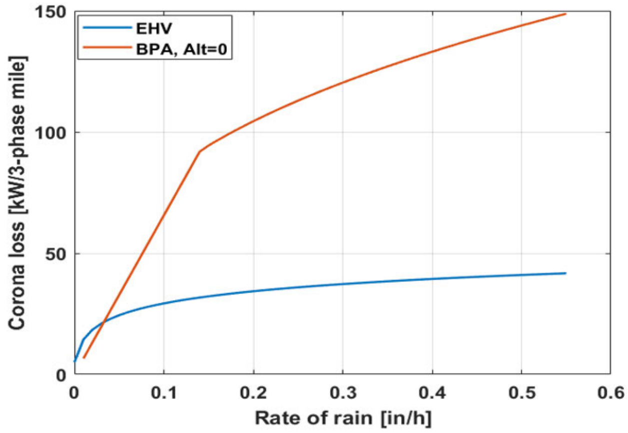

FIGURE 10. **Corona power loss against rain rate for the unconventional HSIL line at an altitude of 0 m using Eqs. (2) and (3).**

E. AUDIBLE NOISE (AN)

The empirical formula by BPA for calculating the average rain audible noise (AN) level (L_{50}) caused by transmission lines with 3 or more subconductors per phase depends on the mean of maximum subconductor surface electric field in each

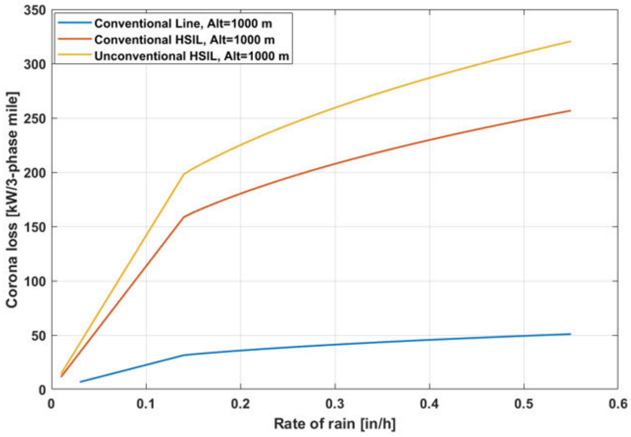

FIGURE 11. Corona power loss against rain rate for different lines at an altitude of 1000 m.

phase, $E_{am}(n)$, d, N, and the distance from each phase, $D(n)$. The net AN level for the line is then given by the sum of AN for each phase, n [21].

$$AN\ (n) = 120 \log_{10} E_{am}\ (n) + 55 \log_{10} d - 11.4 \log_{10} D\ (n) + 26.4 \log_{10} N - 128.4 \qquad (22)$$

The audible noise level for the lines under discussion is independent of frequency. It is shown in Fig. 12. AN is highest for the unconventional HSIL line, which is closely followed by that of the conventional HSIL line. For the conventional line, the peak AN value is around 40 dB at a distance of 10 m from the outer phase and decreases logarithmically with increasing distance. This profile analysis was conducted for the conventional line and the unconventional HSIL line in [22] as well. However, in this instance, we have compared our results to the ones from the Corona and Field Effects program by BPA, and the obtained solutions are much closer to these.

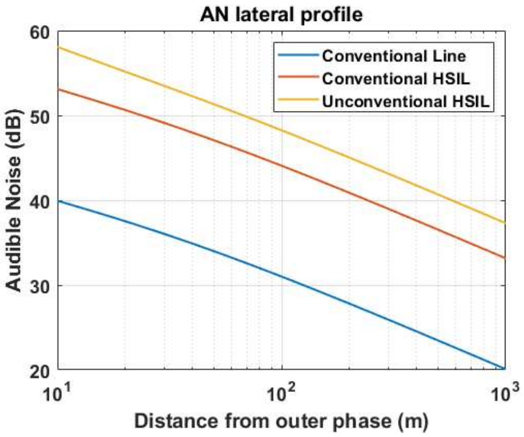

FIGURE 12. Audible Noise (AN) levels up to 1000 m for different overhead transmission lines.

F. RADIO INTERFERENCE (RI) AND TELEVISION INTERFERENCE (TVI)

Radio interference (RI) and television interference (TVI) are also calculated using the BPA formulae [15], [23].

$$RI = 46 + 120 \log_{10}\left(\frac{E_{max}}{17.56}\right) + 40 \log_{10}\left(\frac{2r}{3.51}\right) + RI_f + RI_D + K_A \qquad (23)$$

$$TVI_p = 10 + 120 \log_{10}\left(\frac{E_{max}}{16.3}\right) + 40 \log_{10}\left(\frac{2r}{3.04}\right) + 20 \log_{10}\left(\frac{75}{f}\right) + F_2\ (x) + K_A \qquad (24)$$

Here, r is the radius of the subconductors, RI_f and RI_D are RI correction factors for measurement frequencies different from 1 MHz and the reference parameters respectively, $F_2(x)$ is a function of the radial distance from the conductors, and K_A is a correction factor for the altitude respectively.

Fig. 13 shows the radio interference (RI) levels for detection frequencies of 0.5 MHz, 5 MHz, and 20 MHz respectively.

Fig. 14, in the same way, shows the television interference (TVI) levels for frequencies of 75 MHz, 250 MHz, and 1000 MHz, respectively. It is readily seen that the RI and TVI levels decrease with an increase in frequency.

In Figs. 13 and 14, it can be seen that going from the conventional to the conventional HSIL and the unconventional HSIL lines, the effect of interference increases for each of the frequencies considered. While this happens, it is also apparent for both the HSIL lines that the numerical RI and TVI values are close. The conventional HSIL line is an established one in China [11]. In the USA, the minimum recommended SNR for allowable signal reception is 24 dB for signals above 54 dB. Thus, for the case of RI, it can be understood from Fig. 14 that a signal level of approximately 94 dB should suffice for $f = 0.5$ MHz, and this value is much lower for the remaining frequency levels [24]. For TVI, if the signal sent has a minimum SNR of 40 dB, an acceptable level of signal reception is achieved. Thus, for $f = 75$ MHz, as the maximum noise level is about 20 dB, a signal strength of 60 dB suffices for an allowable signal reception. For $f = 250$ MHz and $f = 1000$ MHz, the required minimum signal strength is much lower.

G. SHIELDING WIRE LOCATION

Lightning strikes are one of the significant operational and environmental risks associated with transmission lines. These strikes can induce extremely high transient voltages and currents in the transmission line, potentially leading to insulation failures, equipment damage, and even catastrophic outages. Properly designed shielding wires can help mitigate the effects of lightning strikes by providing a low-impedance path for the lightning current to safely dissipate to the ground, thereby reducing the risk of damage to the transmission line and associated infrastructure. Thus, effective shielding wire design is essential for mitigating these challenges

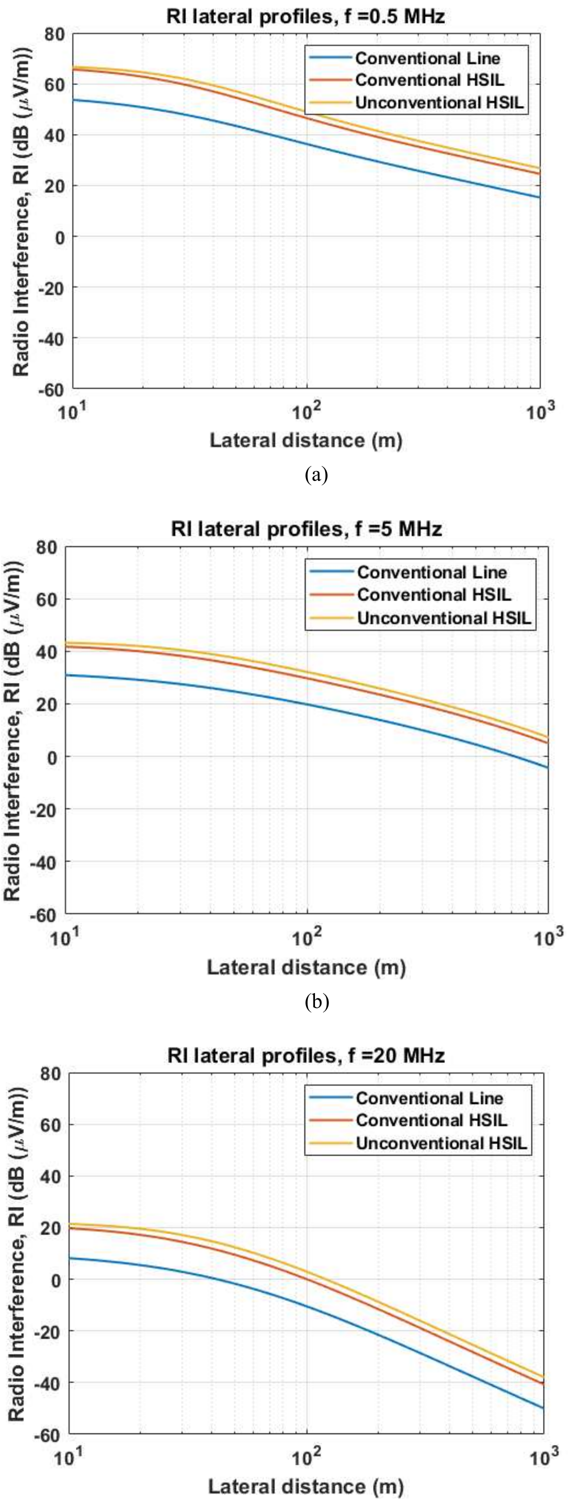

(a)

(b)

(c)

FIGURE 13. RI levels for different transmission lines under (a) $f = 0.5$ MHz, (b) $f = 5$ MHz, and (c) $f = 20$ MHz.

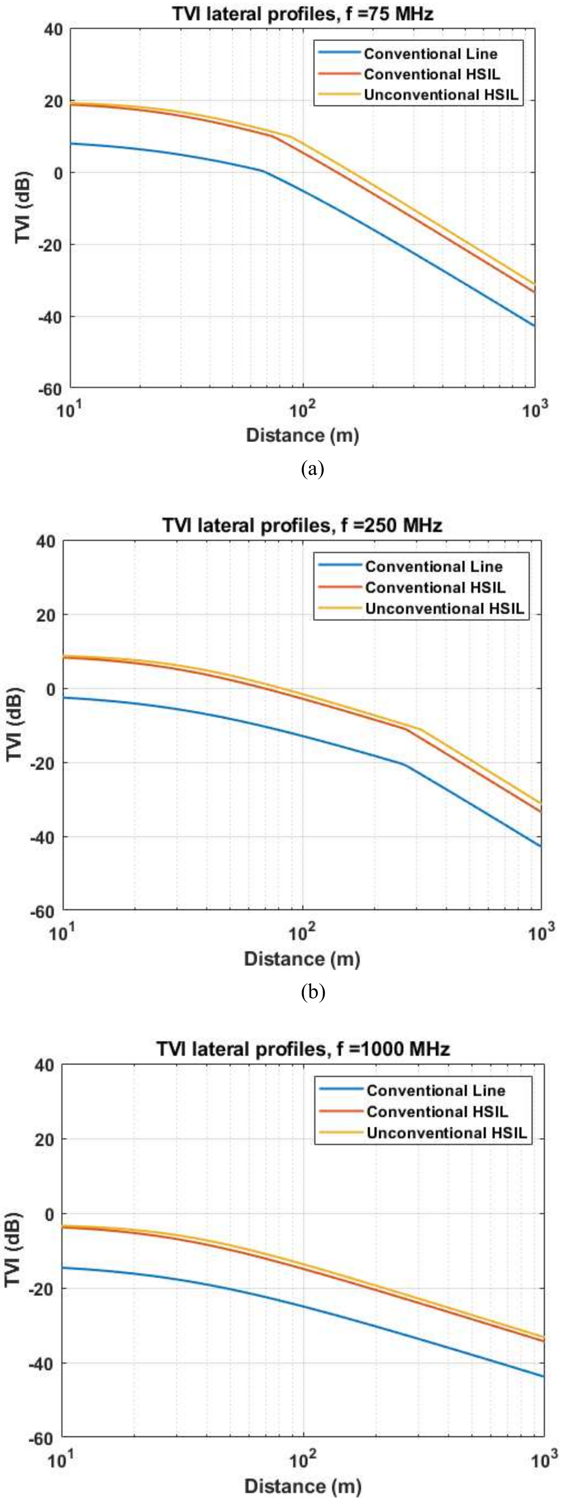

(a)

(b)

(c)

FIGURE 14. TVI levels for different transmission lines under (a) $f = 75$ MHz (b) $f = 250$ MHz (c) $f = 1000$ MHz.

by providing enhanced protection against electrical surges. In this section, the shielding wire location has been determined for the unconventional line shown in Fig. 3e to cover the design shielding wires for our new line design in this paper as well.

The optimal location of the shield wires for the mentioned line has been obtained according to the stroke mechanism of lightning and the results have been analyzed using the value of shielding failure rate (SFR) and shielding failure flashover rate (SFFOR) [25], [26]. SFR is defined as the number of strokes that terminate on the phase conductor per 100 years. The empirical formula for SFR is:

$$SFR = 2N_gL\int_3^{I_m} D_cf(I)dI \tag{25}$$

where N_g represents ground flash density, L (km) represents length of the line, D_c (km) represents the exposure distance for the phase conductor, I_m (kA) represents maximum current at and above which no stroke will be incident on the phase conductor. The minimum stroke current, set at 3 kA, is denoted as the lower limit for the probability density function, $f(I)$ [26], representing the occurrence of lightning current. But not all the strokes are responsible for flashovers. Flashover occurs when the voltage induced by a stroke on the conductor exceeds the minimum voltage leading to a flashover known as critical flashover (CFO). The number of strokes on the phase conductors that result in a flashover is known as SFFOR. The phenomenon of flashover in electrical systems is influenced by a variety of atmospheric conditions, the physical state of equipment, insulating gases, and external environmental factors. Atmospheric conditions such as humidity, temperature, and pressure play a significant role in determining the behavior of insulation materials [27]. High humidity can lead to moisture absorption by insulating surfaces, reducing their effectiveness, while temperature variations can cause expansion or contraction of materials, impacting their structural integrity and insulation performance under high voltage stress. The physical state of equipment, including the type, condition, and design of insulating materials, is equally critical. Environmental exposure, mechanical stress, operational wear, and the accumulation of contaminants like dust or oil can weaken insulation strength and create conductive paths that increase the risk of flashover. Insulating gases, which are integral to electrical systems, also affect flashover thresholds based on their dielectric properties. Gases with lower dielectric strength are more prone to failure under electric stress, highlighting the importance of optimal gas composition in high-voltage equipment. Additionally, external factors such as altitude and atmospheric pressure influence the dielectric breakdown voltage of air and insulating materials. At higher altitudes, decreased air density lowers the breakdown strength of air, making flashover more likely unless equipment is specifically designed to accommodate these conditions. In summary, the interplay between atmospheric variables, the physical state of the equipment, insulating gases, and environmental factors collectively determines the risk of flashover. Recognizing and addressing these dependencies is essential in the design, maintenance, and operation of electrical systems to ensure their reliability and safe performance under varying conditions. In summary, while the interplay between atmospheric variables, the physical state of equipment, insulating gases, and environmental factors collectively determines the risk of flashover, our study focuses specifically on determining the optimal location of the shield wire for the designed transmission line. To find the equation of SFFOR, we need to change the lower limit of the current integral since SFFOR will only require the current responsible for flashover. Thus, SFFOR can be expressed as follows:

$$\begin{aligned}\mathrm{SFFOR} &= 2N_gL\frac{D_{cc}}{2}\int_{I_c}^{I_m} f(I)dI\\ & 2N_gL\frac{D_{cc}}{2}P\left(I_c \le I \le I_m\right)\\ &= 2N_gL\frac{D_{cc}}{2}\left[F\left(I_m\right) - F\left(I_c\right)\right]\\ &= 2N_gL\frac{D_{cc}}{2}\left[Q\left(I_c\right) - Q\left(I_m\right)\right]\end{aligned} \tag{26}$$

Here, N_g represents ground flash density and expressed as, $N_g = 0.04T_d^{1.25}$. I_c represents the critical current threshold for flashover, determined by CFO and the surge impedance of the phase conductor, $Z_c(\Omega)$ as follows:

$$I_c = \frac{2\,(\mathrm{CFO})}{Z_c} \tag{27}$$

where, CFO = 605 (kV/m) × minimum striking distance [25]. The function $Q\,(I)$ depends on the current range, as detailed in Table 5.

TABLE 5. Expression of $Q\,(I)$ for different ranges of current.

I	Equation
3 to 20	$Q = 1 - 0.31e^{-\frac{z^2}{1.6}}$
20 to 60	$Q = 0.5 - 0.35Z$
60 to 200	$Q = 0.278e^{-\frac{z^2}{1.7}}$

The empirical formula for SFFOR relies on numerous line parameters that are essential for determining SFFOR. This paper elaborates on the specific parameters crucial for calculating SFFOR, utilizing a geometric analysis detailed in Fig. 15.

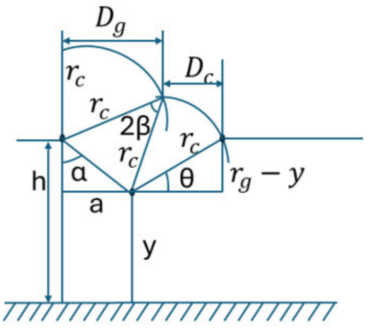

FIGURE 15. Geometrical analysis of shield wires of a transmission line.

In Fig. 16, the geometrical analysis illustrates the relationship between the shield wire and phase conductor of a transmission line. The tower height (h) equals the shield wire height, while y is the height of the phase conductor. α is known as the shielding angle, and from Fig. 15:

$$\alpha = tan^{-1}\frac{a}{h-y} \tag{28}$$

$$\theta = sin^{-1}\frac{r_g - y}{r_c} \tag{29}$$

The distance D_c and D_g are known as the exposure distance for the phase conductor and shield wires, respectively. Their values are derived from the geometrical analysis, expressed as functions of α and θmentioned below:

$$D_c = r_c[cos\theta - \cos(\alpha + \beta)] \tag{30}$$

$$D_g = r_c \cos(\alpha - \beta) \tag{31}$$

The values of r_g and r_c vary based on different empirical formulae presented in [17] and [18]. But among them, the Brown and Whitehead equation is used mostly in shielding analysis, and based on it, the striking distance is expressed as $r = AI^b$. The values of A and b are listed in Table 6 based on the Brown and Whitehead equation.

TABLE 6. Parameter values for the Brown and Whitehead equations.

For r_g		For r_c	
A	b	A	b
6.4	0.75	7.1	0.75

Using the previously mentioned empirical formula, the SFFOR has been determined for the unconventional high natural power line shown in Fig. 3e using Eq. (26) across various shielding angles. To analyze and compare the results the following parameters are chosen in our study:

- The minimum striking distance, which is crucial to computing critical flashover density, was selected as 11.2 feet [26], which is usual for 500 kV lines.
- Two different values for the annual number of thunderstorms, T_d =5 and T_d =30, were considered to represent ground flash density across regions with varying levels of lightning activity. Typically, T_d =5 is indicative of areas with low lightning activity, while T_d =30, is more representative of regions with nearly high levels of lightning activity.
- The height of the tower was calculated based on the coordinates of the subconductors presented in Fig. 3e. To calculate the average height, the shield wire sag was set at 11.25 m [26]. So, the average height: $h = y_A + \left(2/3\right)(11.25) = 39.5$ m
- The SFFOR, measured as flashovers per 100 kilometers per year, was selected to remain within 0.05. In practical applications to serve critical loads, it is preferable to keep the acceptable SFFOR within this threshold of 0.05 per 100 kilometers per year [25], [26].

Fig. 15 illustrates the SFFOR plot for all vertical phases. Observing the plot, it is evident that SFFOR values remain consistent for phases A and B (located at a higher height), whereas it is lower for Phase C.

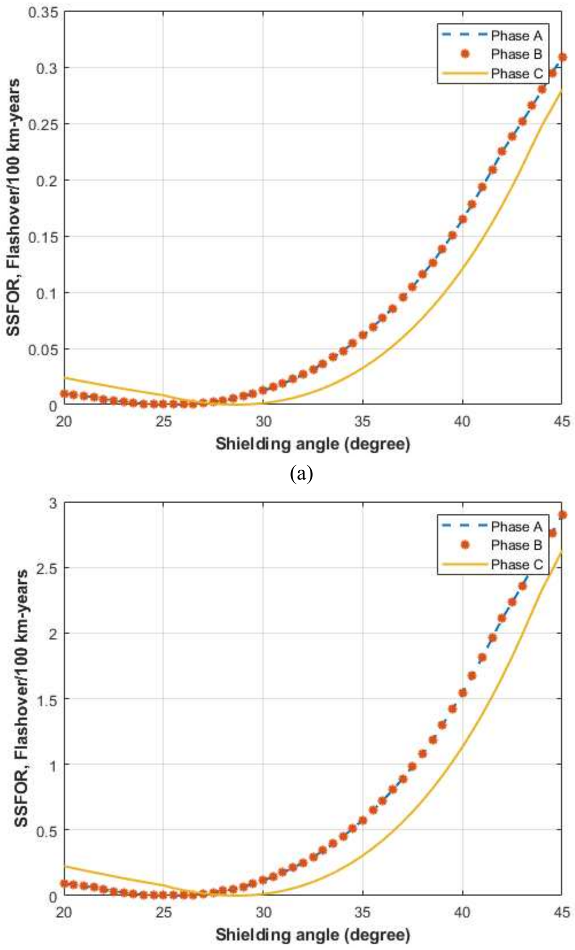

FIGURE 16. SFFOR for all vertical phases (a) T_d =5, (b) T_d =30.

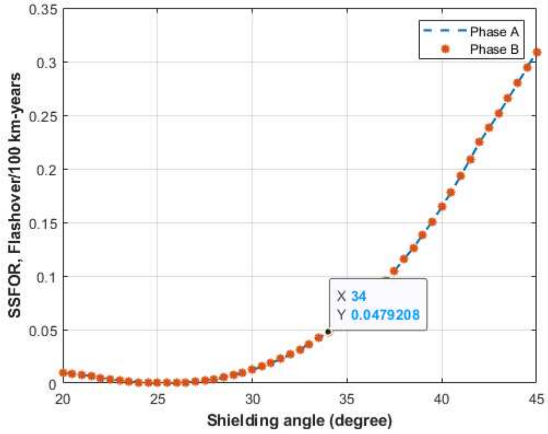

FIGURE 17. SFFOR at different shielding angles of the unconventional line shown in Fig. 3e for Phases A and B for T_d =5.

As a closer view, Fig. 17 shows SFFOR against shielding angles for both phases A and B, indicating a shielding angle of 34° leads to SFFOR of 0.05. Fig. 18 ascertains that for a shielding angle of 34°, SFFOR remains below 0.05 for phase C as well.

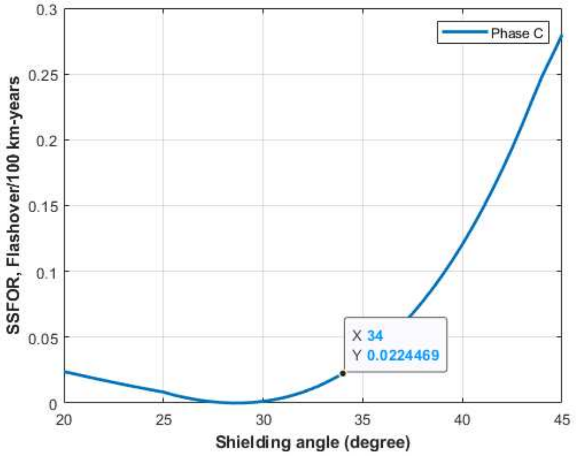

FIGURE 18. SFFOR at different shielding angles of the unconventional line shown in Fig. 3e for Phase C for T_d =5.

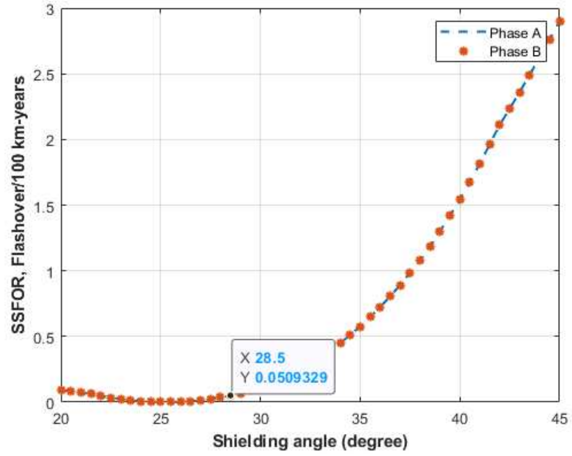

FIGURE 19. SFFOR at different shielding angles of the unconventional line shown in Fig. 3e for Phases A and B for T_d =30.

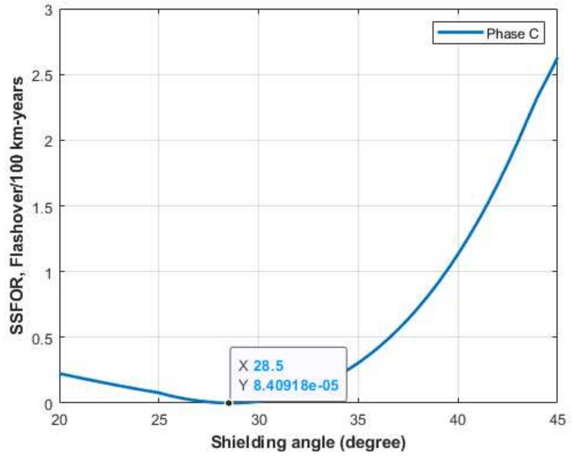

FIGURE 20. SFFOR at different shielding angles of the unconventional line shown in Fig. 3e for Phase C for T_d =30.

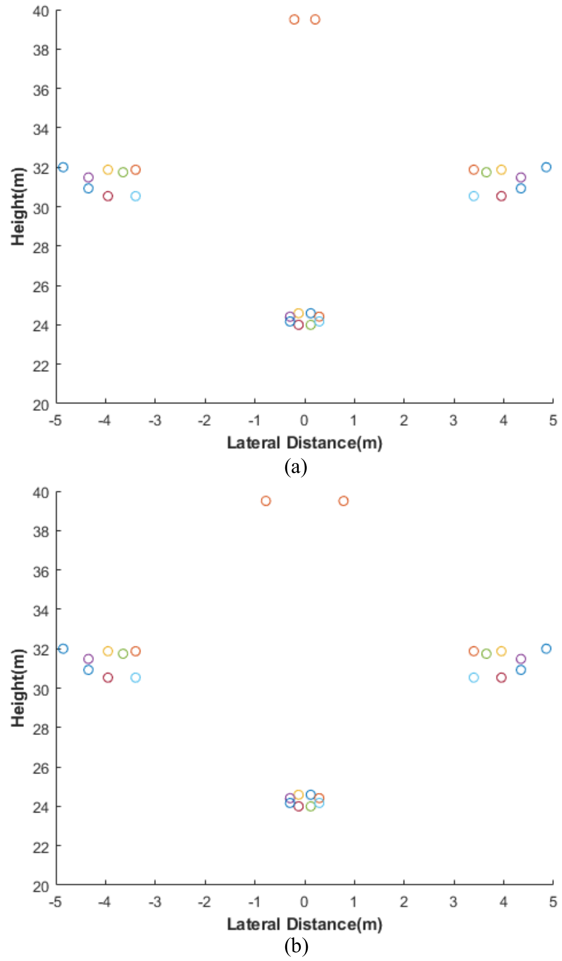

(a)

(b)

FIGURE 21. The whole geometry of the proposed unconventional high natural power lines including phase conductors and shield wires for (a) T_d =5, (b) T_d =30.

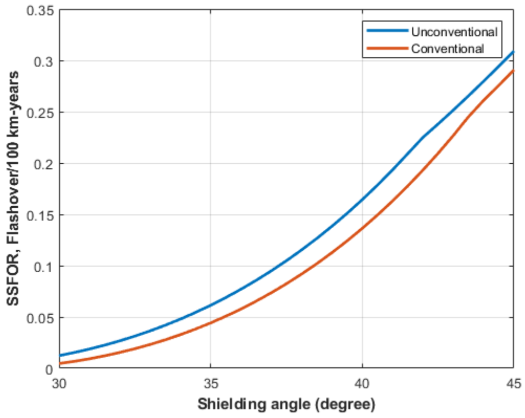

FIGURE 22. SFFOR vs. shielding angle for the conventional line, Fig. 2a, and unconventional high natural power line, Fig. 3e, for T_d =5.

Thus to meet SFFOR $<=0.05$ flashovers/100 km-years for all phases, the shielding angle should be 34°, then the distance between the shield wires for low lightning activity, T_d =5 can be calculated using Eq. (28)

$$\tan 34^{\circ} = \frac{4.85191 - \frac{S_g}{2}}{39.5 - 32} \Longrightarrow \frac{S_g}{2} = 0.21\ m \Longrightarrow S_g = 0.42\ m$$

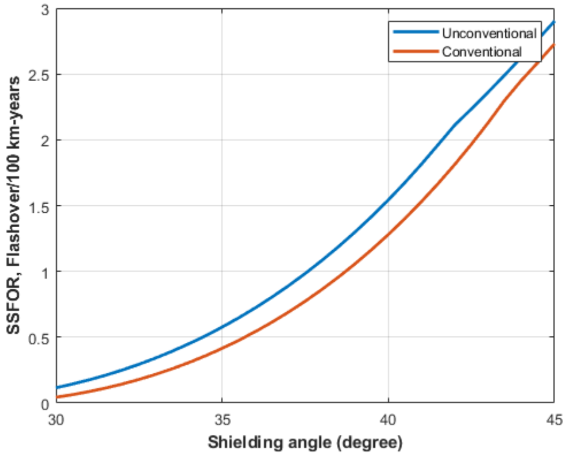

FIGURE 23. **SFFOR vs. shielding angle for the conventional line, Fig. 2a, and unconventional high natural power line, Fig. 3e, for T_d =5.**

Accordingly, for high lightning activity, T_d =30, the plot is shown in Figs. 19 and 20. In this case, the shielding angle for both phases A and B was found to be 28.5°, where SFFOR is at 0.05. Furthermore, Fig. 20, displaying the plot for phase C, validates that for this angle, the SFFOR remains below 0.05 for phase C as well. Thus, the distance between the shield wires for this case will be:

$$\tan 28.5^\circ = \frac{4.85191 - \frac{S_g}{2}}{39.5 - 32} \Longrightarrow \frac{S_g}{2} = 0.78\ m$$
$$\Longrightarrow S_g = 1.56\ m$$

Figs. 21a and 21b show the location of shield wires for T_d =5 and T_d =30, respectively. Figs. 22 and 23 compare the results with the conventional line. For the unconventional novel line, SFFOR values show a slightly high trend but remain within the acceptable limit of 0.05.

V. CONCLUSION

The paper presented optimally designed unconventional designs for transmission lines leading to much higher natural power and much lower line width than conventional lines and conventional high natural power lines. Different electrical aspects of the line design, including magnetic and electric fields under transmission lines, corona loss, audible noise, and radio and television interferences for these newly designed lines, were studied and compared with the conventional line. Moreover, the location of shielding wires for these new lines was studied. It should be noted, however, that mechanical and structural aspects also need to be studied when proposing a new line configuration. Also, we are aware that other electrical aspects, like live line working and challenges when dealing with wind, ice/snow, etc., also need to be investigated. However, we believe this paper provided a good foundation for designing unconventional lines and opened new windows for further research.

REFERENCES

[1] M. Ghassemi, "High surge impedance loading (HSIL) lines: A review identifying opportunities, challenges, and future research needs," *IEEE Trans. Power Del.*, vol. 34, no. 5, pp. 1909–1924, Oct. 2019.

[2] B. Dhamala and M. Ghassemi, "An extra-high voltage test system for transmission expansion planning studies considering single contingency conditions," *Electronics*, vol. 13, no. 19, p. 3937, Oct. 2024.

[3] (May 1, 2024). *MISO Transmission Cost Estimation Guide for MTEP24*. [Online]. Available: https://cdn.misoenergy.org/MISO%20Transmission%20Cost%20Estimation%20Guide%20for%20MTEP24337433.pdf

[4] B. Dhamala and M. Ghassemi, "Smart transmission expansion planning based on the system requirements: A comparative study with unconventional lines," *Energies*, vol. 17, no. 8, p. 1912, Apr. 2024.

[5] B. Dhamala and M. Ghassemi, "Comparative study of transmission expansion planning with conventional and unconventional high surge impedance loading (HSIL) lines," in *Proc. IEEE Power Energy Soc. Gen. Meeting (PESGM)*, Jul. 2024, pp. 1–5.

[6] M. A. Khan and M. Ghassemi, "A new method for calculating electric field intensity on subconductors in unconventional high voltage, high power density transmission lines," in *Proc. IEEE Conf. Electr. Insul. Dielectric Phenomena (CEIDP)*, Oct. 2023, pp. 1–4.

[7] G. N. Alexandrov, *Design of Compacted UHV Transmission Line*. Moscow, Russia: Energoatomizdat, 1993.

[8] M. A. Khan and M. Ghassemi, "A new unusual bundle and phase arrangement for transmission line to achieve higher natural power," in *Proc. North Amer. Power Symp. (NAPS)*, Oct. 2023, pp. 1–5.

[9] R. G. Olsen and C. Zhuang, "The spatial distribution of electric field as a unifying idea in transmission line design," *IEEE Trans. Power Del.*, vol. 34, no. 3, pp. 919–928, Jun. 2019.

[10] *BOLD*. Accessed: Oct. 10, 2024. [Online]. Available: https://www.boldtransmission.com/

[11] H. Wei-Gang, "Study on conductor configuration of 500 kV chang-fang compact line," *IEEE Trans. Power Del.*, vol. 18, no. 3, pp. 1002–1008, Jul. 2003.

[12] P. S. Maruvada, A. Turgeon, and D. L. Goulet, "Study of population exposure to magnetic fields due to secondary utilization of transmission line corridors," *IEEE Trans. Power Del.*, vol. 10, no. 3, pp. 1541–1548, Jul. 1995.

[13] R. G. Olsen, S. L. Backus, and R. D. Steams, "Development and validation of software for predicting ELF magnetic fields near power lines," *IEEE Trans. Power Del.*, vol. 10, no. 3, pp. 1525–1534, Jul. 1995.

[14] E. Arafat, B. Porkar, and M. Ghassemi, "Electric field calculation and comparative analysis of conventional and unconventional transmission lines," *IEEE Access*, vol. 12, pp. 178038–178046, 2024.

[15] *AC Transmission Line Reference Book—200 KV and Above*, EPRI, Palo Alto, CA, USA, 2005.

[16] P. S. Maruvada, *Corona Transmission Covering the Subject From Three Types of Lines*. Sandton, South Africa: Eskom Holdings Ltd, 2011.

[17] P. S. Maruvada, *Corona Performance of High-Voltage Transmission Lines*. New York, NY, USA: Research Studies Press Ltd, 2000.

[18] V. L. Chantier, "Empirical expressions for calculating high voltage transmission corona phenomena," in *Proc. 1st Annu. Seminar Tech. Career Program Prof. Engineers*. Portland, OR, USA: BPA, 1983, pp. 75–82.

[19] J. G. Anderson, M. Baretsky, and D. D. MacCarthy, "Corona-loss characteristics of EHV transmission lines based on project EHV research," *IEEE Trans. Power App. Syst.*, vol. PAS-85, no. 12, pp. 1196–1212, Dec. 1966.

[20] M. A. Khan and M. Ghassemi, "Corona loss calculation for unconventional high surge impedance loading transmission lines," in *Proc. North Amer. Power Symp. (NAPS)*, Oct. 2023, pp. 1–6.

[21] M. G. Combes, R. E. Carberry, V. L. Chartier, P. S. Maruvada, and J. R. Stewar, "A comparison of methods for calculating audible noise of high voltage transmission lines," *IEEE Trans. Power App. Syst.*, vol. PAS-101, no. 10, pp. 4090–4099, Oct. 1982.

[22] M. A. Khan and M. Ghassemi, "Calculation of audible noise and radio interference for unconventional high surge impedance loading (HSIL) transmission lines," in *Proc. IEEE Conf. Electr. Insul. Dielectr. Phenomena (CEIDP)*, Oct. 2023, pp. 1–4.

[23] R. G. Olsen, *High Voltage Overhead Transmission Line Electromagnetics*, vol. 2, 2nd ed., 2018.

[24] R. D. Begamudre, *Extra High Voltage AC Transmission Engineering*. Tunbridge Wells, U.K., 2013.

[25] *IEEE Guide for Improving the Lightning Performance of Transmission Lines*, IEEE Standard 1243-1997, 1997.

[26] A. R. Hileman, *Insulation Coordination for Power Systems*. Boca Raton, FL, USA: CRC Press, 2018.
[27] Z. G. Datsios, P. N. Mikropoulos, and T. E. Tsovilis, "Estimation of the minimum shielding failure flashover current for first and subsequent lightning strokes to overhead transmission lines," *Electric Power Syst. Res.*, vol. 113, pp. 141–150, Aug. 2014.

MUSHFIQUL ABEDIN KHAN (Graduate Student Member, IEEE) received the B.S. degree from Bangladesh University of Engineering and Technology (BUET), Bangladesh. He is currently pursuing the Ph.D. degree in electrical engineering with The University of Texas at Dallas, TX, USA.

EASIR ARAFAT (Graduate Student Member, IEEE) received the B.S. degree from Bangladesh University of Engineering and Technology (BUET), Bangladesh. He is currently pursuing the Ph.D. degree in electrical engineering with The University of Texas at Dallas, TX, USA. His primary research interests include optimization and machine learning to focus on high voltage, insulation aging, power systems design, and grid stability.

SAIKAT CHOWDHURY (Member, IEEE) received the B.S. degree from Bangladesh University of Engineering and Technology (BUET), Bangladesh. He is currently pursuing the Ph.D. degree in electrical engineering with The University of Texas at Dallas, TX, USA. His primary research interest includes electrical insulation for transportation electrification.

MONA GHASSEMI (Senior Member, IEEE) received the Ph.D. degree (Hons.) in electrical engineering from the University of Tehran, Tehran, in 2012.

From 2013 to 2015, she was a Postdoctoral Fellow with NSERC/Hydro-Québec/UQAC Industrial Chair on Atmospheric Icing of Power Network Equipment (CIGELE), University of Québec at Chicoutimi (UQAC), Chicoutimi, QC, Canada. She has been a Registered Professional Engineer, since 2015. She was also a Postdoctoral Fellow with the University of Connecticut, Storrs, CT, USA, from 2015 to 2017. In 2017, she joined the Bradley Department of Electrical and Computer Engineering, Virginia Tech, Blacksburg, VA, USA, as an Assistant Professor. In 2021, she was named both the Steven O. Lane Junior Faculty Fellow and the College of Engineering Faculty Fellow of Virginia Tech. In 2022, she joined the Department of Electrical and Computer Engineering, The University of Texas at Dallas as an Associate Professor. She has authored more than 200 peer-reviewed journal and conference papers and one book chapter. Her research interests include electrical insulation materials and systems, high voltage/field engineering and technology, power systems, and plasma science. She was a member of the Nominations and Appointments Committee of the IEEE Dielectrics and Electrical Insulation Society (DEIS) and the At-Large Member of the Administrative Committee of the IEEE DEIS. She is the Vice-President (Technical) of IEEE DEIS, a DEIS Representative of the IEEE USA Public Policy Committee on Transportation and Aerospace Policy (CTAP) and USA Technology Policy Council Research and Development Policy Committee, a DEIS Technical Committee Member on Dielectrics and Electrical Insulation for Transportation Electrification, and a member of the Education Committee of IEEE DEIS. She received the Chairholder of the Texas Instruments Early Career Award, from 2022 to 2028. She received the three most prestigious and competitive career awards: the Department of Energy Early Career Research Program Award, the National Science Foundation CAREER Award, and the Air Force Office of Scientific Research Young Investigator Research Program Award. She received the 2020 Contribution Award from IET High Voltage and four Best Paper Awards. She is an Associate Editor of IEEE TRANSACTIONS ON DIELECTRICS AND ELECTRICAL INSULATION, IEEE TRANSACTIONS ON INDUSTRY APPLICATIONS, *IET High Voltage*, *International Journal of Electrical Engineering Education*, and *Power Electronic Devices and Components*, a Guest Editor of *Aerospace* and *Energies*, and an Associate Guest Editor of IEEE JOURNAL OF EMERGING AND SELECTED TOPICS IN POWER ELECTRONICS.

• • •